KPFM visualisation of the Schottky barrier at the interface between gold nanoparticles and silicon

Luis Lechaptois, Yoann Prado, Olivier Pluchery

Published in ***Nanoscale***, 2023, **15**, 7510-7516
https://doi.org/10.1039/D3NR00178D

ARTICLE

KPFM visualisation of the Schottky barrier at the interface between gold nanoparticles and silicon

Luis Lechaptois[a, b], Yoann Prado [a] and Olivier Pluchery*[a]

Abstract: Gold nanoparticles (AuNPs) deposited on a doped silicon substrate induce a local band bending and a local accumulation of positive charges in the semiconductor. Unlike the case of planar gold-silicon contacts, working with nanoparticles results in reduced values for the built-in potential and lower Schottky barriers. Here, AuNPs of 55 nm diameter were deposited on several silicon substrates that were previously functionalized with aminopropyltriethoxysilane (APTES). The samples are characterized by Scanning Electronic Microscope (SEM) and the nanoparticle surface density is assessed with dark-field optical microscopy. A density of 0.42 NP/µm² was measured. Kelvin Probe Force Microscopy (KPFM) is used to measure the contact potential differences (CPD). The CPD images exhibit a ring-shape pattern ("doughnut-shape") centred on each AuNP. The built-in potential is measured at +34 mV for *n*-doped subtrates and decreases to +21 mV for *p*-doped silicon. These effects are discussed using the classical electrostatic approach.

Introduction

Schottky contact occurs when a metal and a semiconductor are in contact and when their respective work functions are different, the metal one being larger.[1] This phenomenon is well established since the years 1920ies following the work of W.H. Schottky and plays a fundamental role for controlling the electric current in electronic devices, for triggering the transfer of electron in catalysis or enabling the current onset in photovoltaic cells.[2] The Schottky barrier reflects a special distribution of charges near the interface that spans over the space charge region (SCR) on the semiconductor side. It is responsible for the onset of a rectifying current. Even if the qualitative behaviour is well documented, the exact calculation of the barrier height is still under debate[3]. Moreover, when dealing with nanostructures, such as metallic nanoparticles in contact with a semiconducting surface, this barrier is even less predictable because the nanoparticles are already significantly charged when their size is small, which profoundly modifies their apparent work function.[4–6] Moreover their work function also depends on their diameters.[5–7] Yet, predicting the presence of a Schottky barrier and the height of this barrier in case of nanoparticles has become an important topic.[8] A renewed interest is also coming from the field of photocatalysis, where gold nanoparticles are often used for injecting hot electrons into a semiconductor substrate and for triggering chemical reactions.[9–11]

Gold nanoparticles (AuNPs) are also used for nanoelectronics devices where an electrical contact between a gold nanostructure and semiconductor is sought: this is essential to properly assess whether the contact is ohmic or Schottky-type (rectifying)[1]. In such investigations, Kelvin Probe Force Microscopy (KPFM) reveals as a key instrument, since it allows measuring the variations of the local work function through the contact potential difference (CPD) for individual nanostructures.[2,12] It was recently applied for AuNPs on TiO_2 by several groups.[9–11,13–15] In the present article, we use KPFM for analysing the geometry of the Schottky barrier formed by 55 nm AuNPs grafted on silicon with either *n*- or *p*-doping. This is a model system that shed light on the mechanism of Schottky barrier formation for nanostructures. Our results show that the KPFM image exhibits ring-shaped CPD features that reflects the local band bending induced in the *n*-doped silicon substrate by the spherical nanoparticles. The barrier height is strongly reduced with a *p*-doped silicon, as expected from the Mott-Schottky model. A model is discussed.

Experimental

Materials

For our experiments, *n*-doped (doped with phosphorus) and *p*-doped (doped with boron) silicon wafers were cut into 1 x 1 cm² pieces with a diamond tip. *n*-doped silicon wafers <100> with a dopant concentration of 10^{14} - 10^{15} cm^{-3} (1-10 Ω.cm) and *p*-doped silicon wafers with a dopant concentration of 10^{14} - 10^{15} cm^{-3} (10-20 Ω.cm), were purchased from ITME. MiliQ water (18.3 MΩ.cm) was used for solution preparation and rinses. 3-aminopropyltriethoxysilane (APTES) was purchased from

[a] *Institut des NanoScience de Paris, Sorbonne University, CNRS, UMR7580, 4 place Jussieu, 75005, Paris, France*
[b] *Slim Lab, Nanyang Technological University, 70 Nanyang Drive, Singapore*
* Corresponding author: olivier.pluchery@insp.jussieu.fr.
Electronic Supplementary Information (ESI) available: SEM images; KPFM images acquired with different parameters (other scan speeds and other lift scan heights); KPFM images of the APTES layer; KPFM images for *p*-doped substrates; statistical analysis of the values of the built-in potential for *n*-doped and *p*-doped substrates; calculated band diagrams for some junctions of interest.

Published in ***Nanoscale***, 2023, **15**, 7510-7516
https://doi.org/10.1039/D3NR00178D

Aldrich and methanol from VWR Chemicals. AuNPs of 50 nm diameter used for this study were synthesised following the seeded-growth method explained by Bastús *et al.*[16] and they are stabilized by citrate molecules.

Silicon surface chemistry and gold nanoparticles grafting

First, silicon samples were cleaned with acetone and ethanol under sonication and dried under nitrogen flow. Next, they were dipped into an APTES:methanol solution (volumic ratio 1:10) for 2h, followed by three successive rinses in methanol under sonication in order to remove the excess of APTES. The functionalized samples were dried under a nitrogen flow. One drop of AuNPs suspension was drop-casted onto each of the four silicon samples with an increasing deposition time: 1 min (sample A), 2 min (sample B), 10 min (sample C) and 40 min (sample D). Finally, the samples were thoroughly rinsed with ultra-pure water and dried under a nitrogen flow.

Characterization techniques

Kelvin Probe Force microscopy (KPFM)

Kelvin Probe Force Microscopy is an advanced technique based on the Atomic Force Microscopy (AFM). It measures the local variations of the surface potential by detecting the contact potential differences (CPD) between a sample and a conductive AFM probe. It produces a CPD map. More precisely, when the tip of the probe is brought close to the surface, Fermi levels align as a result of charge transfer. The electric charges are reorganized between the tip and the sample and the CPD builds up (denoted V_{CPD}). The CPD causes the onset of an electrical force that is nullified by applying an external bias (V_{DC}) with the same magnitude as the V_{CPD}. The applied external bias is equal to the difference of work functions between the tip ($\mathrm{WF_{tip}}$) and the sample ($\mathrm{WF_{sample}}$), defined as:

$$V_{DC} = V_{CPD} = \frac{\mathrm{WF_{sample}} - \mathrm{WF_{tip}}}{|q|} \quad (1)$$

where q the charge of the electron. Therefore, it is possible to determine the local work function of the sample surface knowing the work function of the tip.[17] Beware that in some setups, V_{DC} is applied to the tip, then $V_{DC} = -V_{CPD}$. Topography and CPD of our samples have both been measured using a *Bruker Multimode* 8 AFM. For KPFM experiments, we used a silicon cantilever and the tip is coated with Pt-Ir to make it conductive. Here, SCM-PITv2® probes from Bruker were used. The radius of the tip was 25 nm. The cantilever of this probe has a resonance frequency f_0 = 75 kHz and a spring constant k = 3 N.m^{-1}. Topography was measured by *PeakForce Tapping*® technique where the tip periodically approaches the sample until the force setpoint is reached. CPD is measured in the Amplitude Modulation (AM) mode. Topography and CPD were acquired within two passes above the surface. The tip performs a first pass recording the topography, then lifts up at a given Lift Scan Height (LSH) and acquires the CPD, following the recorded topography of the first pass (see Fig. 1). Values for LSH between 20 nm and 70 nm were used, and the best results were obtained with LSH = 60 nm (See discussion below for details). Experiments were carried out at a slow rate (0.15Hz/line or 750 nm/s) for images of 1024 x 1024 pixels. Higher scan rates (2250 nm/s and 3000 nm/s) were also tested and they gave the same results (see Fig. S2 in the S.I.). Since these high scan rates lead to a higher probability of the tip crashing into irregularities of the sample, we maintained 0.15 Hz/line in our experiments.

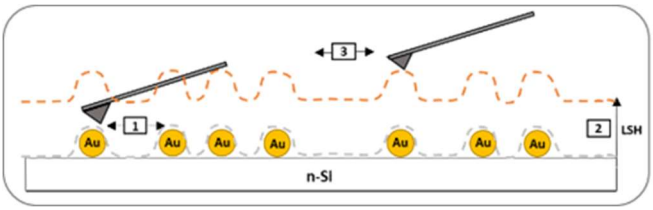

Figure 1: KPFM measurement principle; **Step 1**: the surface topography is acquired with the *PeakForce Tapping®* mode during a first pass (grey dash line) over one line; **Step 2**: the cantilever ascends to the pre-defined lift scan height (LSH); **Step 3**: the cantilever follows the previously recorded surface topography along the same line and above the sample. It constantly adjusts the value of V_{DC} for cancelling the tip-sample electrostatic force (orange dash line).

Optical microscopy

Optical images were recorded in a dark-field (DF) mode with a *Nikon Eclipse LV100ND* microscope using a *TU Plan Fluor 100x* objective (Numerical Aperture = 0.90) with a *Universal Epi-illuminator* that enables dark-field observation in reflection. 70 x 50 µm² images are recorded with an integration time of 2 s and show the scattering patterns of the AuNPs on silicon. Scanning Electon Microscopy (SEM) images are obtained with a *Zeiss Supra 40* instrument.

Results and discussion

Microscopy measurements

The SEM image in Fig. 2 shows a 2 x 1.5 µm² area of sample A. The size distribution of the AuNPs has been measured from five different images from the same sample and on 116 nanoparticles in total (see inset in Fig. 2). More SEM images are shown in Fig. S1 of the SI. We measured an average diameter of 55 ± 10 nm. A small number of AuNPs are found to be aggregated on the surface, as shown in Fig. 2. Dark-field optical microscopy images of samples A, B, C and D were recorded and are shown in Fig. 3. These images exhibit clear bright and green spots that are caused by the optical scattering of AuNPs. This allows a rapid estimation of the surface coverage with AuNPs as long as the AuNPs are not too close to each other. We see an increase of the AuNP coverage on the silicon from sample A to sample D as the time of deposition increases. The density of AuNPs was computed as follows: 0.42 NP/µm² for 1 min, 0.50 NP/µm² for 2 min, 0.94 NP/µm² for 10 min and more than 1.0 NP/µm² for 40 min. In order to perform a meaningful analysis of the CPD induced by AuNPs, we seek samples with well separated nanoparticles. On the basis of the DF images, we select the sample A and will concentrate on this sample in the following.

Published in ***Nanoscale***, 2023, **15**, 7510-7516
https://doi.org/10.1039/D3NR00178D

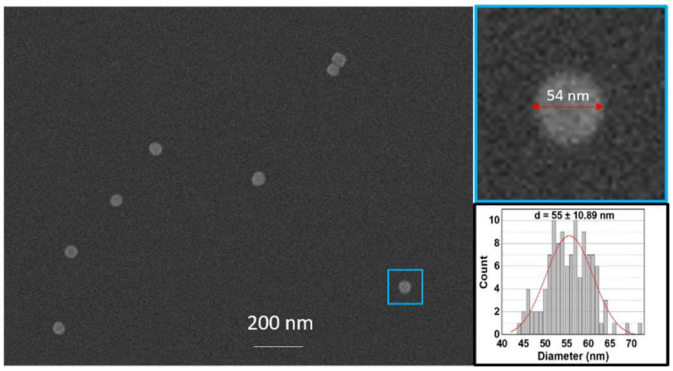

Figure 2: SEM image of gold nanoparticles deposited on an *n*-doped silicon wafer, that was previously functionalized with APTES. The lower inset shows the size distribution of the particles with an average diameter of 55 ± 10 nm.

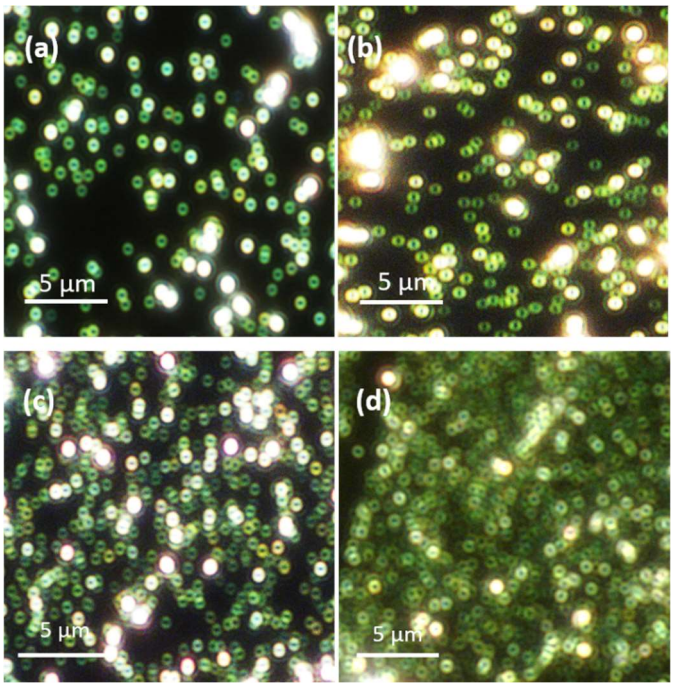

Figure 3: Dark-field optical microscopy images (20 x 20 µm²) of AuNPs drop-casted on *n*-doped silicon wafer for various times: (a) Sample A, 1 min; (b) Sample B, 2 min; (c) Sample C, 10 min; and (d) Samples D, 40 min. Light scattered by AuNPs exhibits a typical ring-shaped pattern (see text).

Interestingly, we notice in the DF images of Fig. 3, that AuNPs appear with a green scattering pattern that has a diameter of about 850 nm and above all, that they exhibit a ring or *doughnut* shape. According to *Chen et al.*, the ring shape of the dark-field scattering pattern is due to the interaction between the substrate and the nanoparticles.[18] In fact, when AuNPs are excited by light, their localized surface plasmon resonance (LSPR) behaves like a dipole which is oriented parallel or perpendicular to the surface, depending on the orientation of the excitation electric field (which in turn is related to the illumination geometry of the dark-field microscope). This dipole induces an image dipole in the substrate and both coupled together. When the excitation electric field is parallel to the surface, the LSPR dipoles presents a radiation pattern with a torus shape whose plane is oriented perpendicular to the substrate. It is detected as a bright solid spot. Conversely, when the excitation field is perpendicular to the substrate, the dipolar radiation pattern is a torus oriented parallel to the surface and is detected as a ring-shaped spot. Then, the total intensity of the dark-field scattering pattern will be the sum of the contribution from the dipole and its image. For the parallel one, its image is opposite to the original and so they will cancel each other partially. On the other hand, the perpendicular one is along the same direction as its image leading to an increase of the net dipole. Since, the coupling intensity of the radiation and their images is strongly dependant on the dielectric constant of the substrate, when the dielectric constant increases, the magnitude of the coupling increases too. In the present study, silicon has a high dielectric constant leading to the decrease of the parallel radiation intensity and increase of the perpendicular one. It results in a ring-shaped scattering pattern on silicon. However, when these AuNPs are deposited on glass, we measured a regular circular pattern and not a ring-shaped one.[18]

Kelvin Probe Force Microscopy measurements

One typical topography image obtained with KPFM on sample A shows a portion of image with seven AuNPs in Fig. 4-a. The diameters of the nanoparticles measured from the heights acquired in AFM, are between 51 and 61 nm, which is consistent with the SEM images. The lateral apparent diameter of the AuNP was measured on 12 nanoparticles and the average value was found to be 90 nm, which is higher than the height due to the convolution with the tip. The APTES monolayer also exhibits small aggregates of typically 1 nm and up to 8 nm that were easily distinguished from AuNPs. The corresponding CPD variations were below 1 mV and will be not discussed further because they cannot be confused with AuNPs (see an illustration in Fig. S4 of the SI). Fig. 4-b displays the CPD image of these seven AuNPs. The CPD rises from −808 mV on the silicon substrate up to −777 mV close to the AuNPs. The close-up image in Fig. 4-d shows that the CPD adopts a ring pattern with a diameter of 120 nm, that exhibits some similarities with the DF images, but for completely different reasons as explained further on. In order to rule out the probability that the ring patterns were due to a convolution artefact, additional measurements were carried out at higher scan rates (see Fig. S2 in the SI) and at different LSH. Actually, when the LSH is lower than 40 nm, the CPD becomes unstable and inaccurate probably because the tip intermittently contacted the nanoparticle during the second pass (see SI Fig. S3). As long as the LSH is greater than 40 nm, the CPD images consistently exhibit a ring-shaped pattern. Thee CPD reaches its maximum value at the edge of the ring and a minimum value at its centre, which is 10 mV below these edges. Fig. 4-e and 4-f display the CPD profiles across such ring. Similar results can be observed for AuNPs deposited on *p*-doped silicon showing also a ring-shaped CPD pattern but less pronounced (see SI Fig. S5). More precisely, Fig. 4-e shows the overlap of the topography (black

Published in ***Nanoscale***, 2023, **15**, 7510-7516
https://doi.org/10.1039/D3NR00178D

line) and the CPD (red line). It shows that the increase of the CPD occurs above the interfaces between the AuNP and the doped silicon, and that the central drop occurs when the tip is above gold. These results reveal the existence of a potential barrier when scanning from silicon to gold with a barrier height given by the difference of the CPD measured above the junction Si/Au ($\Phi_{junction}$ =-777 mV on Fig.4-e) and above the silicon (Φ_{Si}= -808 mV). Such a potential rise (ΔCPD = $\Phi_{junction}$ - Φ_{Si}) was measured for a large number of AuNPs on *n*-doped silicon substrates as well as for *p*-doped substrates. We have measured that the potential rise is higher for AuNPs on *n*-doped silicon than on *p*-doped silicon. Potential barriers were measured for 32 different AuNPs and show an average potential rise of 34.3 ± 0.6 mV for the *n*-doped and 21.2 ± 1.0 mV for *p*-doped (See SI Fig. S6).

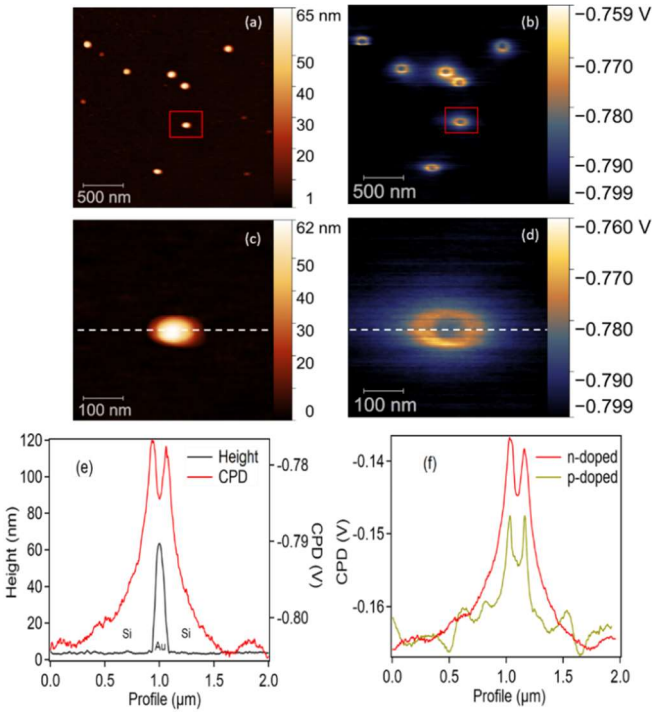

Figure 4: Topography images (a, c) and their corrsponding CPD images (b, d) of gold nanoparticles on *n*-doped silicon (Sample A) measured by KPFM. (e) Profile of the height (black line) and of the CPD (red line) for one single AuNP (profile taken along the white dash lines). (f) CPD profiles for one AuNP on an *n*-doped (red) and a *p*-doped (green) sample. Notice that the *n*-doped curve was shifted vertically to align with the *p*-doped curve for the sake of comparison.

Discussion

Band bending at an ideal planar interface

The intimate contact between a gold contact and silicon, generates a Schottky contact. It results in a local charge reorganization and the built-up of a local electric field (linked to the so-called *built-in* potential). Since the work function of gold ($q\Phi_{Au}$) is higher than that of silicon ($q\Phi_{Si}$), electrons tend to accumulate at the metal surface, whereas holes spread next to the semiconductor surface. Charge neutrality requires that positive and negative charges are equilibrated. Since the carrier concentration is relatively low on the semiconductor side, the positive charges are distributed over a rather large barrier region of width W_D, which is the depletion region or space charge region (SCR). (see reference textbooks *e.g.* Sze[1]). Therefore, the potential energy of an electron on the silicon side ($x > 0$) writes:

$$E(x) = q\Phi_{Si} - \frac{q^2 N_D}{\varepsilon_S}\left(W_D x - \frac{x^2}{2}\right) \qquad \text{if } 0 \le x \le W_D$$

and $$E(x) = q\Phi_{Si} \qquad \text{if } x > W_D \qquad (2)$$

Here *q* is the elementary charge, N_D (m^{-3}) is the semi-conductor dopant concentration, and ε_S (F.m^{-1}) is the silicon permittivity. All the quantities are expressed within the S.I. unit system.

The variation of the electron energy in the semiconductor is the *band bending*. This potential energy is equal to the work function and is equal to the CPD measured in our experiments within one additional constant linked to the work function of the tip of the KPFM. W_D is calculated by solving the Poisson equation and is related to the built-in potential Φ_{bi} according to the equation (3):[1]

$$W_D = \sqrt{\frac{2\varepsilon_S}{qN_D}\left(|\Phi_{bi}| - \frac{kT}{q}\right)} \qquad (3)$$

The corresponding energy band diagram is represented in Fig. 5-a and shows the progressive band bending of an amount of Φ_{bi} over the distance W_D. The CPD profile shown in Fig. 4-e corresponds to this evolution and is going to be discussed more in depth in the following. The Schottky barrier height (SBH) is noted $\Phi_{B,n}$ for the *n*-doped silicon in Fig. 5, and can be calculated according to Equation (4) for a semiconductor surface without surface states (ideal case):

$$\Phi_{B,n} = \Phi_{bi} + \Phi_n \qquad (4)$$

where Φ_n is the potential difference between the conduction band and the Fermi level E_F.

$$\Phi_n = kT.ln\frac{N_C}{N_D} \qquad (5)$$

where N_C is the effective conduction band density of states at 300 K, $N_C = 3.2 \cdot 10^{19} cm^{-3}$. The calculation yields: Φ_n = 270 mV for the dopant concentration N_D = 10^{15} cm^{-3} used in our experiments. Temperature is set at *T* = 300 K for all the calculations.

In *p*-doped semi-conductor, holes in the valence band are the majority carriers and they usually control the electrical current once in contact with a metal. In this case, a Schottky contact appears when the Fermi level of the metal (Φ_m) is lower than the semi-conductor one (Φ_S): the bands bend downward and a Schottky barrier for holes $\Phi_{B,p}$ appears. On the other hand, when $\Phi_m > \Phi_S$, bands bend upwards and $\Phi_{B,p}$ = 0. The contact

Published in ***Nanoscale***, 2023, **15**, 7510-7516
https://doi.org/10.1039/D3NR00178D

is ohmic. From the results shown in Fig. 4-f, the CPD profile for *p*-doped silicon shows an upward band bending corresponding to an ohmic contact. Though, a band bending with a potential barrier ($\Phi_{bi} = 21\ mV$) is still detected by KPFM for the *p*-doped substrate. The value of this barrier is lower than the one obtains on *n*-doped silicon ($\Phi_{bi} = 34\ mV$).

If we consider this ideal planar model, the values of the built-in potential and the SBH can be easily computed. Calculations are carried out with the software *Band Diagram Program* developed by Knowlton[19,20] that solves the Poisson equation as briefly explained above. With an Au/*n*-Si junction that includes a 2 nm SiO_2 layer (thermal oxide layer used *as-received*) this calculation yields: Φ_{bi} = 660 mV and W_D = 910 nm. The SBH is $\Phi_{B,n}$ = 930 mV. More details can be found in Fig. S7 of the SI. However, the calculated value of Φ_{bi} is far greater than the 30 mV measured in our experiments. And so is the calculated SBH for *n*-doped silicon compared to the 10 mV obtained with KPFM.

Actually, in the case of nanoparticles, band bending occurs not at a planar interface but at a sphere-plane interface. We need to refine the model and consider that AuNPs and silicon surfaces have only one point of contact (right under the nanoparticle). This is the topic of the following section.

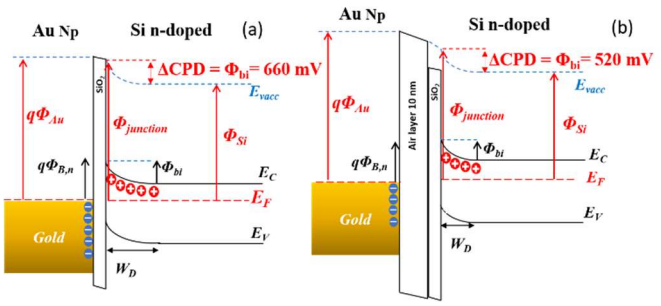

Figure 5: Schematic of band bending when gold and n-doped silicon are in direct contact (a) and in contact across a 10 nm air layer (b). SiO_2 native oxide layer is represented on top of the silicon wafer with a thickness of 2 nm.

Calculation of the band bending at the sphere-plane interface

We now consider the spherical AuNP on the planar silicon substrate and use the polar coordinates centred on the AuNP as shown in Fig. 6. Only along a vertical line ($\theta = 0°$) gold is in direct contact with the silicon surface. For other angles, there is a gap of air between gold and silicon noted d_{air}. Therefore, the band bending induced by the AuNP can be calculated by varying the polar angle θ between −90° and +90°. The case $\theta = 0°$ (d_{air} = 0 nm) was already calculated in the previous section and the following values were computed for the *n*-doped silicon: Φ_{bi} = 660 mV and W_D = 910 nm. At $\theta = 45°$, geometrical considerations directly yield d_{air} = 10 nm as shown in Figure 6. These calculations are illustrated in Fig. 5-b and yield Φ_{bi} = 520 mV and W_D = 800 nm (See also in the SI, Fig. S7). Fig. 6 shows the variation of the SCR for all the possible angles. The orange area represents the geometry of the depletion layer induced below the AuNP and where positive charges accumulate. Interestingly for $\theta > 86°$, this model shows that there is a limit over which there is no more electrostatic influence of the AuNP on the silicon, and over which the SCR vanishes to zero. This limit corresponds to d_{air} = 320 nm. This value gives an order of magnitude of the tip-nanoparticle distance under which a CPD change is expected. Actually, Fig. 4-d shows that the CPD starts increasing in a circular area of radius between 200 and 300 nm, in agreement with this limit of d_{air} = 320 nm. Regarding the values for Φ_{bi}, our calculations are only indicative and cannot reproduce the exact values of the built-in potential and the SBH. One issue is the convolution of the CPD profile with the finite value of the radius of the KPFM tip. Fig.7 shows an approached CPD profile that mimics the convolution of the CPD profile with a spherical tip of radius 25 nm. The initial band bending is 46 mV and the convolution leads to a reduction down to 35 mV. This calculation also shows that the SBH is reduced from 66 mV to 20 mV.

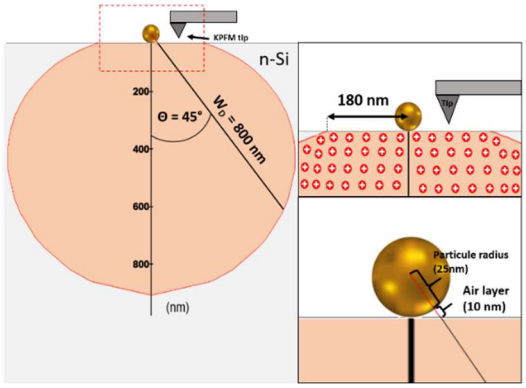

Figure 6: Graph of depletion layer lengths W_D calculated in function of the angle θ (°). Each angle corresponds to an air layer thickness. At θ = 45°, the air layer is 10 nm and W_D = 800 nm.

Finally, this study shows that on a silicon doped with N_D = 10^{15} cm^{-3}, a 50 nm AuNPs induces a ring-shaped space charge region that is positively charged and that spreads some 200 nm around the nanoparticle. It results in a local increase of the surface potential of at least 34 mV. Previous work from *Wang et al.* also showed a ring-shaped pattern of the CPD for AuNPs deposited on TiO_2 substrate. They measured a 30 mV potential barrier.[10] Other authors studied 100 nm TiO_2 nanoparticles deposited on Pt, and show that the Schottky barrier height is reduced of 300 mV by the presence of an insulating layer[21]. However, no clear explanation of the ring pattern in the CPD images were provided.

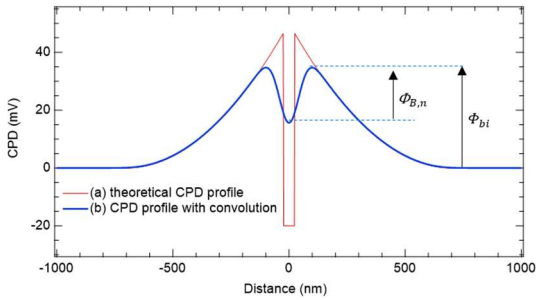

Figure 7: Simulated CPD profiles of an AuNPs/n-Si junction: ideal profile (red) and profile including the effect of the tip convolution (blue). For a 50 nm AuNP, the resulting Schottky barrier height is $\Phi_{B,n}$ = 20 mV and the built-in potential is Φ_{bi} = 35 mV.

Conclusions

In this study, we have investigated how 55 nm AuNPs deposited on a doped silicon surface induce charge transfer and how KPFM data reveal the band bending in the silicon. It shows up as ring-shaped patterns of 120 nm diameter around AuNPs in the CPD images, where the CPD rises of 34 mV for *n*-doped substrates and of 21 mV for *p*-doped (dopant concentration 10^{15} cm^{-3} in both cases). This circular area probed by KPFM is a visualization of the space charge region which is positively charged in the case of Au-Si interface at equilibrium (no external bias was applied). A simple model based on solving the Poisson equation, shows that the Schottky barrier height is evaluated at 300 mV in the case of spherical AuNPs on *n*-Si, which turns to be much lower than in the case of the traditional planar junction Au-Si (SBH = 930mV). With our KPFM measurements we have detected the SBH as 10 mV dip in the centres of the ring patterns in the CPD images. This low value is caused by the limited lateral resolution of KPFM since the CPD results from the convolution of the potential variation and the curvature of the tip. This detection of the positive charges gathered next to the AuNPs, even at equilibrium opens new perspectives for understanding the reactivity of AuNPs and other metallic nanoparticles on semiconductors. These positive charges (holes) around the AuNPs can interact with adsorbed species and be used for different applications such as photocatalysis or chemical reactions.[8,21] Moreover, knowing the value of the SBH and the band bending area, is of great interest for understanding how hot carriers can be generated using the plasmonic properties of AuNPs on doped silicon substrate.[13,15,22,23]

Author Contributions

L. Lechaptois: methodology, investigation and writing.
Y. Prado: investigation and resources.
O. Pluchery: conceptualization, methodology, funding acquisition and writing.

Conflicts of interest

There are no conflicts to declare.

Acknowledgements

KPFM acquisitions were carried out at the Advance Atomic Force Microscopy platform (advAFM) of Sorbonne Université. Special acknowledgements go to Hervé Cruguel for technical support.
LL acknowledges the financial support from the Joint PhD programme Sorbonne University – Nanyang Technological University. OP thanks Ianina Lucila Violi for fruitful and insightful discussions.

Notes and references

1 S. M. Sze and K. K. Ng, *Physics of semiconductor devices*, Wiley-Interscience, Hoboken, NJ, Third edition., 2007.
2 J. Llacer, D. Moerman, O. Douhéret, X. Noirfalise, C. Quarti, R. Lazzaroni, D. Théron and P. Leclère, *ACS Appl. Nano Mater.*, 2020, **3**, 8268–8277.
3 R. T. Tung and L. Kronik, *Phys. Rev. B*, 2021, **103**, 035304.
4 S. Stehlik, T. Petit, H. A. Girard, J.-C. Arnault, A. Kromka and B. Rezek, *Langmuir*, 2013, **29**, 1634–1641.
5 Y. Zhang, O. Pluchery, L. Caillard, A.-F. Lamic-Humblot, S. Casale, Y. J. Chabal and M. Salmeron, *Nano Lett.*, 2015, **15**, 51–55.
6 Y. Zhang, J. Kang, O. Pluchery, L. Caillard, Y. J. Chabal, L.-W. Wang, J. F. Sanz and M. Salmeron, *ACS Appl. Nano Mater.*, 2019, **2**, 4711–4716.
7 D. M. Wood, *Phys. Rev. Lett.*, 1981, **46**, 749–749.
8 G. Žerjav, M. Roškarič, J. Zavašnik, J. Kovač and A. Pintar, *Appl. Surf. Sci.*, 2022, **579**, 152196.
9 E. Kazuma and T. Tatsuma, *Adv. Mater. Interfaces*, 2014, **1**, 1400066.
10 S. Wang, Y. Gao, S. Miao, T. Liu, L. Mu, R. Li, F. Fan and C. Li, *J. Am. Chem. Soc.*, 2017, **139**, 11771–11778.
11 Y. Gao, W. Nie, Q. Zhu, X. Wang, S. Wang, F. Fan and C. Li, *Angew. Chem.*, 2020, **132**, 18375–18380.
12 P. Knotek, T. Plecháček, J. Smolík, P. Kutálek, F. Dvořák, M. Vlček, J. Navrátil and Č. Drašar, *Beilstein J. Nanotechnol.*, 2019, **10**, 1401–1411.
13 A. Jian, K. Feng, H. Jia, Q. Zhang, S. Sang and X. Zhang, *Appl. Surf. Sci.*, 2019, **492**, 644–650.
14 H. Lee, Y. Hong, D. Lee, S. Hwang, G. Lee, J. Yang and D. S. Yoon, *Nanotechnology*, 2020, **31**, 215706.
15 L. Hammoud, C. Strebler, J. Toufaily, T. Hamieh, V. Keller and V. Caps, *Faraday Discuss.*, 2023, 10.1039.D2FD00094F.
16 N. G. Bastús, J. Comenge and V. Puntes, *Langmuir*, 2011, **27**, 11098–11105.
17 W. Melitz, J. Shen, A. C. Kummel and S. Lee, *Surf. Sci. Rep.*, 2011, **66**, 1–27.
18 H. Chen, T. Ming, S. Zhang, Z. Jin, B. Yang and J. Wang, *ACS Nano*, 2011, **5**, 4865–4877.
19 R. G. Southwick and W. B. Knowlton, *IEEE Trans. Device Mater. Reliab.*, 2006, **6**, 136–145.
20 R. G. Southwick, A. Sup, A. Jain and W. B. Knowlton, *IEEE Trans. Device Mater. Reliab.*, 2011, **11**, 236–243.
21 T. Ano, F. Kishimoto, S. Tsubaki, Y.-H. Lu, J. N. Hohman, M. M. Maitani, M. Salmeron and Y. Wada, *J. Phys. Chem. C*, 2021, **125**, 13984–13989.
22 X. Zhang, Y. L. Chen, R.-S. Liu and D. P. Tsai, Rep. Prog. Phys., 2013, 76, 046401.
23 M. J. Kale, T. Avanesian and P. Christopher, *ACS Catal.*, 2014, **4**, 116–128.